

Calculation of Neutron Yields Released by Electrons

Incident on Selected Materials*

William P. Swanson

Stanford Linear Accelerator Center

Stanford, California 94305

ABSTRACT

Calculations are described of yields of low-energy neutrons released by electrons incident on semi-infinite slabs of natural C, Al, Fe, Ni, Cu, Ag, Ba, Ta, W, Au, Pb and U, for all incident electron energies. Yields are based on photon differential track length distributions derived for thick targets from Approximation B of analytical shower theory, with additional corrections for electron and photon propagation in the materials. The track length distributions are folded together with published photoneutron cross sections by numerical integration. When referred to unit incident electron beam power, the yield of each material exhibits a sigmoid behavior, rising from threshold to approach a constant saturation value. At high electron energies, the average trend of the neutron yield is given by $9.3 \cdot 10^{10} Z^{(0.73 \pm 0.05)} \text{ neutrons s}^{-1} \text{ kW}^{-1}$. Quantitative comparison is made to yields obtained in a separate calculation in which Approximation A is substituted for Approximation B. Comparison is made to published calculations and measurements, and radiation protection implications are discussed.

*Work Supported by Department of Energy
Submitted to Health Physics

INTRODUCTION

Apart from bremsstrahlung, neutrons constitute the most hazardous secondary radiation produced by electrons as they strike targets at energies above the photoneutron threshold. Almost all research electron accelerators operate at energies at which copious yields of photoneutrons can be produced. In addition, there has been considerable recent interest in the significance of the neutron dose equivalent imparted by medical accelerators. For these reasons it is important to have reliable predictions of neutron yields released as electrons strike various target materials. Furthermore, an understanding of the systematics of neutron production by electrons is invaluable to those involved in radiation protection planning at electron accelerators. This paper describes estimates of neutron yields from thick targets in which essentially all of the energy of the electromagnetic cascade initiated by an incident electron is absorbed.

From the outset, it must be understood that the electrons directly release relatively few neutrons; the most copious yields are produced by the interaction of photons, which are emitted by the electrons in an electromagnetic cascade within the target. The energy range close to the photoneutron threshold is especially difficult to treat because the photoneutron cross sections are rapidly varying and the photon track length distribution is not easy

to estimate accurately without Monte Carlo calculations; the electron energy approaches or is even less than the material's critical energy and photons tend to penetrate media considerably more easily than at much higher energies. For these reasons the simplifications of Approximation A of analytical shower theory (Ro41, Ro52) are not adequate, and a procedure was developed by which the photon track length in various materials could be analytically obtained with an accuracy comparable to that of the measured photoneutron cross sections. It was also desired that the method conveniently give predictions for a wide range of materials in arbitrarily small energy intervals in order that systematics could be studied and comparison with experiment and other estimates could be easily made without the expense and complication of Monte Carlo calculations.

The geometry considered is one in which an electron of initial energy E_0 is incident on a slab of material thick enough that virtually all of the energy of the ensuing electromagnetic cascade is absorbed. While we consider the target to be thick with respect to electromagnetic radiation, we disregard the attenuation of the neutrons within the same target. The resulting quantities will then represent photoneutron source terms which may be used for the planning of radiation protection. The neutron shielding effect of the target may be taken into account as a separate step, if this is believed warranted.

The photoneutron yield is obtained by the convolution

of the photoneutron production cross section (including factors for neutron multiplicity) and the photon differential track length, (*) multiplied by other factors

(*) The differential track length $dL/dE(E)$ is defined as that function of energy E which, when multiplied by an increment in energy ΔE , gives the incremental track length ΔL of all particles of a given type whose energy is in the interval $(E, E + \Delta E)$. In computing the differential track length in this context, an integration over the entire volume of the medium and over all shower generations is implied, and electrons and positrons are treated alike as a single kind of particle.

which are constants for each material (Table 1):

$$Y(E_0) = \frac{N_0 \rho}{A} \int_{k_{th}}^{E_0} \sigma_n(k) \frac{dL^\gamma}{dk}(E_0, k) dk \quad , \quad (1)$$

where $Y(E_0)$ is the number of neutrons produced per incident electron, E_0 is the incident electron kinetic energy, N_0 is Avogadro's number, ρ is the material density, A the atomic weight, k the photon energy, dL^γ/dk the photon differential track length and $\sigma_n(k) = \sigma(\gamma, n) + \sigma(\gamma, np) + 2\sigma(\gamma, 2n) + \dots$. The photoneutron threshold energy k_{th} lies in the range 6 - 13 MeV for most materials, and all of the photoneutron cross sections go through a peak due to a process generally known as the

"giant resonance." (See, for example, Be75, Fu76.) The cross sections used in the calculation are parameterizations of cross sections obtained with quasi-monoenergetic photons given in the compilation by Berman (Be76). Above 25 - 30 MeV, the cross sections of Jones and Terwilliger (Jo53) are used.

PHOTON TRACK LENGTH

As a first step in obtaining the photon differential track length, the electron differential track length dL^e/dE is calculated for each material using Approximation B of analytical shower theory, as given by Tamm and Belenky (Ta39):

$$\frac{dL^e}{dE}(E_0, E) = \frac{E_0 X_0}{0.437 \epsilon_0^2} \left[\frac{1}{x} - (1+x) e^x \int_x^{x_0} \frac{e^{-s}}{s^2} ds \right], \quad (2)$$

where $x = E / 0.437 \epsilon_0$ and $x_0 = E_0 / 0.437 \epsilon_0$. The symbol X_0 represents the radiation length (i.e., the distance in which an electron's energy is reduced by an average factor of $1/e$ by radiation at the high-energy limit) and ϵ_0 is the critical energy, defined as the energy at which the average energy loss by radiation (per unit length) is equal to the average energy loss by ionization (per unit length). (The values used for calculation differ somewhat from the critical energy so defined. See Table 1 for values of all parameters used.) This formula of Tamm and Belenky (Ta39) is used unchanged in our procedure.

The photon differential track length is based on an integration of dL^e/dE from the photon energy in question k

to the maximum electron energy of the shower E_0 :

$$\frac{dL^\gamma}{dk}(E_0, k) = \frac{F^\gamma X_p}{k X_0} \int_k^{E_0} \frac{dL^e}{dE}(E_0, E) F^e dE \quad (3)$$

The integral of Eq. (3) is multiplied by the factor X_p/X_0 to account for the fact that the photon relaxation length X_p is controlled by the pair-production cross section σ_p at high energies ($X_p^{-1} = N_0 \rho \sigma_p / A$), and is somewhat greater than the radiation length ($X_p/X_0 \approx 9/7$; see Table 1). If the correction factors F^e and F^γ are omitted, Eqs. (2) and (3) are the same as Approximation B of analytical shower theory as formulated by Tamm and Belenky (Ta39; also see Section 5.19 of Ro52). This formulation is similar to Approximation A insofar as it assumes that the pair-production cross section, as well as the electron radiative cross section, are at their respective high-energy limits. The Compton effect is also ignored, but provision is made in Approximation B for constant ionization loss by electrons and this allows the electron differential track length to be reasonably well described down to kinetic energies below the photoneutron thresholds.

However, the photon differential track length in Approximation B will be inaccurate at low energies for two reasons: Firstly, the integral of Eq. 3 without the correction factor F^e assumes that the electron bremsstrahlung cross section is at its asymptotic limit whereas it is really smaller than that in the energy range

considered. The correction factor F^e (Fig. 1) inserted under the integral sign is an attempt to correct for this, and will suppress the photon differential track length by a factor ranging from about 0.7 to 0.9, depending on the energy and material. Values of this factor were derived from tabulations of the electron radiative energy loss of Berger and Seltzer (Be64). Secondly, the photon absorption cross section is not really at the high-energy limit for pair production; the pair production cross section is considerably smaller at low energy, and therefore the photons tend to travel greater average distances. This problem is easily removed by multiplying the integral by another factor F^γ which is the ratio of the photon mass attenuation coefficient of the material at the high-energy limit divided by the same quantity determined at the energy in question k (Ro52, p. 277). That factor, shown in Fig. 2, is an important energy-dependent factor which can raise the photon track length by as much as a factor of 1.5 to 2.5 depending on the energy and the material. Values were derived from the photon mass attenuation coefficients published by Hubbell (Hu69). Both factors illustrated in Figs. 1 and 2 are essential in extending the validity of Approximation B for photons down to energies as low as the photoneutron thresholds for the materials studied.

In Fig. 3, we compare the electron track length for four materials and thereby see the effect of the critical energy ϵ_0 ; because a higher critical energy implies more

ionization loss over the electron's path relative to radiation, the whole distribution is suppressed and flattened as the critical energy is increased. To check the reasonableness of these distributions, the following observations are noted: (a) All distributions correctly show a rise near the maximum energy ($E = E_0$) to a value $dL^e/dE = X_0 / \epsilon_0$. (**)

(**) A helpful explanation of this rise is given by Zerby and Moran (Ze62).

is comparable to the value given by the continuous slowing down approximation (CSDA) in which dE/dL (and therefore dL/dE) is assumed equal to the average for one electron of energy E (Be64). (c) Using the same program, we have also assumed an unrealistically small critical energy (1 MeV) for one trial calculation. The result is consistent with the approach to Approximation A (shown as the straight line with logarithmic slope equal to -2) expected for small ϵ_0/E_0 . (***)

(***) The electron differential track length in Approximation A is $dL^e/dE = 0.437 E_0 X_0 / E^2$. The photon differential track length differs only in the multiplicative constant: $dL^\gamma/dk = 0.572 E_0 X_0 / k^2$.

This means that ϵ_0 has less effect as ϵ_0/E_0 becomes small.

(d) Going to the opposite extreme, we have verified that a

very large ϵ_0 gives an almost constant electron differential length equal to X_0/ϵ_0 . (e) The integral electron track length $L^e = \int dL^e/dE dE$ was evaluated numerically for several cases and found to be comparable to $X_0 E_0/\epsilon_0$, which would be required by conservation of energy.

Once the electron differential track length distribution is known, the photon distribution is obtained from Eq. 3 by numerical integration. The photon distributions at $E_0 = 20$ MeV, corresponding to the electron distributions of Fig. 3 are shown in Fig. 4, where the effect of an increasing critical energy in suppressing these distributions is clearly seen. Figures 5 - 7 show the photon track length distributions for incident electron energies in the range $E_0 = 5 - 35$ MeV for Pb, Cu and Al, respectively. In order to present these distributions clearly on a linear plot, the ordinate scale shows the dimensionless quantity $(k^2/X_0 E_0) dL^\gamma/dk$. With this ordinate scale, Approximation A applies equally to all materials and all E_0 and is plotted at the value 0.572 for comparison. It is apparent that Approximation A completely misses details of the true track length distribution which are significant for all materials in the energy range shown; the initial and final slopes of the distributions and smooth transitions to an upper plateau are not given by Approximation A. For lower-Z materials (Figs. 4, 6, 7), Approximation A also overestimates the track length distribution by a substantial amount.

When plotted in this manner, the curves are quite symmetrical; in the Tamm-Belenky (Ta39) formalism without corrections, the initial rise of all curves is the same and is tangent to the line $(9/7) k/\epsilon_0$. This is a consequence of the fact that in Approximation B the total electron track length is $L^e = X_0 E_0 / \epsilon_0$ for constant loss of energy by ionization at the rate $dE/dX = \epsilon_0/X_0$. Similarly, the slopes of all curves at $k = E_0$ are the same for all incident electron energies and are equal to $-(9/7) (1/\epsilon_0)$. This is borne out in the curves shown and is a consequence of dL^e/dE being equal to X_0/ϵ_0 at $E = E_0$.

An impression of the accuracy of these calculations can be gained by comparison with Monte Carlo calculations made by Alsmiller and Moran (Al66) for 34 MeV electrons incident on $10 X_0$ of Pb (Fig. 5). (Ten radiation lengths is practically equivalent to a semi-infinite target.) The histogram agrees quite well with the calculated 35-MeV distribution in the region of the giant-resonance peak but indicates that the curve is too high for higher photon energies. We may also compare these calculations with Monte-Carlo calculations for 34 MeV electrons incident on a $5-X_0$ Cu target (Fig. 6) and we see that the calculated distribution generally lies above the histogram. This is natural because 5 radiation lengths does not approximate an infinitely thick target very well, but it probably also indicates that the calculated curve overestimates the true track length towards the upper part of the spectrum, just as in Fig. 5.

On Figs. 5 - 7, we also plot the photoneutron cross section (barns) as a function of photon energy. Notice the qualitative differences in shape for different Z; for Pb the peak occurs at about 14 MeV and is quite narrow. The lower-Z materials (Cu, Al) generally have higher thresholds and broader peaks which occur at higher photon energies. Furthermore, the lower-Z materials induce relatively less radiation at low energies (i.e., they have higher critical energies) and therefore all of the track lengths are suppressed relative to Approximation A. From a comparison of Figs. 5 - 7, one can rightly infer that neutron yields would be highest in Pb, intermediate in Cu and smallest in Al.

PHOTONEUTRON YIELDS

Neutron yields obtained by numerical integration of Eqs. 1 and 3 are shown in Fig. 8 for incident electron energies near threshold ($E_0 = 0 - 40$ MeV) for several natural elements representing a wide range of Z. The yields are calculated for these materials taking the proportions of the naturally occurring isotopes into account. The ordinate gives the neutron yield in neutrons per second per kW of incident electron beam power. We choose to normalize to unit beam power rather than current because at high energies all of the curves tend towards constant (saturation) values when presented in this manner; above a certain energy, the neutron yield becomes nearly proportional to the incident

power regardless of the energy per incident particle. Moreover, the kilowatt is a convenient unit with which to specify average beam power at typical existing electron accelerators.

The high-Z materials exhibit the swiftest rise with energy in Fig. 8; the smaller critical energy (Table 1), the larger electron and photon correction factors (Figs. 1, 2), the sharper cross section peak (Figs. 5 - 7) as well as the lower thresholds (Table 1) all contribute to this faster approach to saturation. From inspection of these curves, it appears that the neutron yield per electron beam power is at or above the "shoulder" (****) of the yield

(****) We may conveniently define "shoulder" as the point of each sigmoid where the smallest (most negative) second derivative occurs.

curve if the incident electron energy is about twice the energy k_0 of the giant-resonance peak for the material. For higher-Z materials ($Z \gtrsim 47$), the "shoulder" corresponds to about 75% of the saturation value (Cf. $E_0 = 500, 1000$ MeV, Table 2). In lighter materials ($Z \lesssim 30$) for which ϵ_0 is comparable to, or larger than k_0 , a "shoulder" is less easily distinguished and occurs at a smaller fraction (~50%) of saturation.

These calculations are extended to $E_0 = 100$ MeV in Fig. 9, which confirms that the neutron yield per unit beam power

approaches a plateau with only modest slope if E_0 is more than about twice the energy of the giant-resonance peak. Yields calculated for 500 and 1000 MeV (Table 2) confirm this flattening trend. (*) Apart from uranium, the high-Z

(*) The integration over photon energy extends only to 150 MeV for these higher electron energies, but the effect of this limited range of integration on the calculated yield is negligible. For medium weight nuclei ($A \approx 100$), photons of energy above 150 MeV contribute at most about 1% of the total neutrons, even for infinitely large E_0 . Most of this small fraction are of high energy, and, although very important for high-energy accelerators such as SLAC, are not the subject of this report. See further discussion in section entitled Significance for Radiation Protection.

materials studied give typically $2 \cdot 10^{12}$ neutrons s^{-1} per kW of electron beam power and those of lower-Z give correspondingly less, as anticipated in Figs. 5 - 7.

The present results apply only to slabs of material which are infinitely thick. Information on the dependence of neutron yield on target thickness must be obtained elsewhere (see, for example, Al66, Ba59, Be70, Ha75). Figure 10 shows Monte-Carlo calculations, derived from Alsmiller and Moran (Al66) and Hansen et al. (Ha75), replotted as the relative neutron yield as a function of

target thickness. These curves indicate that in this energy range, the most copious production in a thick, high-Z target occurs at about $1 - 2 X_0$, and about half of the neutrons are produced in the first $2 - 3 X_0$. When rescaled to the absolute yields of Figs. 8 and 9, such curves are useful in estimating neutron yields in thin and intermediate targets.

In Table 2, comparison is made to published measurements and other calculations for thick targets ($\approx 3 X_0$). There are unexpectedly wide variations in these yield determinations, which can be traced mainly to disagreement among older cross section measurements. Because the present calculations are for semi-infinite targets, the most meaningful comparisons of published results with the present calculations are those for very thick targets ($10 - 20 X_0$). A correction factor has been applied in those cases where the published value is for a target less than this. Both the original and corrected values are given in Table 2.

In discussing the accuracy of these results, we distinguish errors arising from the photon track length calculations from those residing in the cross section data. Qualitative comparison with track length distributions for photons published by Alsmiller and Moran (Al66) using Monte-Carlo techniques indicates that for a given E_0 , the method used here tends to overestimate the photon track length towards the upper part of the spectrum (high k) and to underestimate the photon track length at low k (Figs. 5, 6). The same qualitative trend is also observed for Pb at

100 MeV (Al66) and for Cu at 50 and 100 MeV (Ze62, Ga69a). The effect of this on the calculated neutron yield depends on the relationship of the giant-resonance peak to the overall photon distribution. Qualitatively, the errors in the photon differential track length manifest themselves as an overestimate of the neutron yield for all materials in the region of the initial rise with energy (Figs. 8 and 9), a slight underestimate (by 0 - 10%) at saturation, and are correct somewhere just above the "shoulder". The saturation yields ($E_0 = 500, 1000$ MeV of Table 2) are probably accurate to $\pm 10\%$ for all materials, considering only calculational uncertainties. Furthermore, the absolute calculational error over the entire energy range studied is probably within $\pm 10\%$ of the saturation yield for high-Z materials ($Z \gtrsim 50$) and $\pm 15\%$ of the saturation yield for low-Z, with the systematic deviations just noted. This means that the relative uncertainties are larger at E_0 close to threshold, especially on the steeply rising portions of Figs. 8 and 9.

Uncertainties in the measured cross sections on which these results are based probably give rise to no more than $\pm 15\%$ additional relative error at any E_0 . Combining the two types of error in quadrature, the overall accuracy of the saturation yields is probably about $\pm 20\%$, considering both calculational and cross sectional uncertainties.

The experimental results of Barber and George at 34 MeV (Ba59, for Cu, Pb and U, corrected to $10 X_0$ in Table 2) are probably the most direct independent check of these

calculations. They are in excellent agreement for Cu, and are higher for Pb and U by only 9 and 7%, respectively. Measurements by Bathow et al. (Ba67, Te76) at 6.3 GeV indicate saturation yields (of neutrons having energy less than 25 MeV) about double the values calculated in this work, with an error of about $\pm 25\%$. However, the calculation and experiment are only roughly comparable; the experimental setup involved an external bremsstrahlung beam from a synchrotron target, rather than an electron beam, incident on a thick sample. Secondly, the thick sample and detector were placed in a concrete cell so that corrections were required for the background of reflected neutrons.

RELATIONSHIP TO APPROXIMATION A

Frequent use has been made of Approximation A to obtain neutron yield and material activation estimates (De63, Ba67, De68, Ba69, Sw75). Therefore it is interesting to compare the results of the present calculation with what one would obtain from Approximation A:

$$Y(E_0) = 0.572 \frac{N_0 \rho X_0 E_0}{A} \int_{k_{th}}^{E_0} \frac{\sigma_n(k)}{k^2} dk \quad (\text{APPROXIMATION A}), \quad (4)$$

where the symbols have the same meanings as for Eq. 1. The abscissa of Fig. 11 is the atomic number of the material of the target struck by the electron beam and the ordinate is the yield as given by the corrected Approximation B (Eqs. 1 and 3), divided by the yield predicted by Eq. 4. The parameter indicated is the incident electron energy. Owing to the systematic change in giant-resonance parameters with Z, smooth curves can be meaningfully drawn through the points. At lower E_0 , Approximation A generally overestimates the actual neutron yield by a large factor, particularly for low-Z materials. On the other hand, it underestimates the yield at high E_0 for $Z \gtrsim 40$ by as much as a factor of 1.3 - 1.5. (A main source of this deviation is related to the correction factors of Fig. 2.) There is no difference in the calculated points at $E_0 = 500$ and 1000 MeV, and no reason to expect a significant change at higher energies either, because of the weighting of the photon spectrum towards lower energy by the factor k^{-2} in Eq. 4.

Yield estimates using Eq. 4 are quite easy to make for

any material by hand calculation, and a correction factor can be readily interpolated from Fig. 11 to obtain a better approximation to the true yield.

SIGNIFICANCE FOR RADIATION PROTECTION

The utility of Figs. 8 and 9 to the person concerned with the planning of radiation protection for a low-energy electron accelerator is self evident; once the target material, electron beam energy and power are known, the neutron source term can be read directly from these graphs.

It must be understood that the yields given here correspond to a situation in which a thick, single-material target is used. In many cases this is not the actual geometry. Where a thin target of one material is followed by a thick piece of material of different atomic number, the yield may be significantly changed, and an accurate prediction cannot be obtained by the methods described. A combination of a thin, high-Z target followed by a thick lighter material may yield significantly more neutrons than the lighter material would by itself (see, for example, Be70). The converse is also true; an initial low-Z target can be used to reduce the net photon track length so that the neutron yield is suppressed in the high-Z material. It would be conservative radiation protection practice in such cases to assume that the full energy is absorbed only in the highest-Z material that absorbs significant beam energy, and disregard the lighter materials.

In the case of a medical accelerator used for photon therapy, a large fraction of the energy of photons produced in a high-Z target is also absorbed in high-Z materials, primarily the tungsten and/or lead of the fixed collimator and jaws; the remaining energy is absorbed in the compensating filter or is transmitted as the "useful beam". If the compensating filter is also of high-Z material, the neutron yields given here represent a realistic source term for the case where the jaws are completely closed. (Note that the yields for $E_0 = 20 - 25$ MeV (Fig. 8) are quite similar for all high-Z materials studied.) Cases in which the filter is of lower-Z material, or the jaws are not closed, are difficult to treat but it is clear that the yields presented can safely be used as upper limits. The problem of shielding against the neutrons by materials within the treatment unit is a separate problem not addressed here.

Although the low-energy region is emphasized in this report, the results presented give useful estimates of low energy neutron production for accelerator installations of even very high energy, as the giant resonance phenomenon is the most copious source of neutrons from an unshielded electron target, regardless of electron energy. Table 2 shows results of this calculation for the discrete energies $E_0 = 500$ and 1000 MeV. When compared to the 100-MeV results, it is seen that a large change in E_0 excites only a modest increase in yield per unit electron beam power, and

there is little or no change in the range 500 - 1000 MeV. For the higher electron energies, the integration over photon energy is extended only to 150 MeV, because above this the dominant photoneutron production mechanism changes, owing to the onset of photopion production at $E_0 \approx 140$ MeV. Extending the range of integration above 150 MeV would have negligible effect on the calculation because of the very pronounced importance of the giant resonance and the weighting of the photon spectra at lower photon energies by the factor k^{-2} (Cf. Eq. 4). However, with electron accelerators operating much above the photopion threshold ($E_0 \approx 140$ MeV), it is the high-energy neutron component ($E_n \approx 100$ MeV) which is most capable of penetrating thick layers of shielding. In fact, for most such facilities, the low energy neutrons may, to a good approximation, be disregarded in the calculation of the biological shield, because they are readily attenuated compared to high energy neutrons (De68). However, the present results remain valuable as source terms for the calculation of neutron ducting, and as estimates of neutron backgrounds and doses-equivalent near unshielded or thinly shielded targets.

Figure 12 shows the saturation yield of neutrons, plotted against atomic number Z of the target material for $E_0 = 500$ MeV (Table 2). As already seen in Figs. 8 and 9, neutron production generally rises with atomic number. The data points are from the calculations just described and the

straight line, obtained from a least-squares regression, is

$$\begin{aligned} Y(\text{neutrons s}^{-1} \text{ kW}^{-1}) &= \\ & (1.3 \pm 0.2) 10^{12} (Z/37.5)^{(0.73 \pm 0.05)} \\ & = 9.3 10^{10} Z^{(0.73 \pm 0.05)} \end{aligned} \quad (5)$$

for electron beams totally absorbed at high energies. (***)

(***) The first expression is cast in a form in which the fitted parameters are almost independent; the off-diagonal elements of the covariance matrix are zero and interpretation of the uncertainties shown is straightforward. These uncertainties describe the statistical distribution of points and do not reflect the systematic errors discussed in the previous section. For this fit, Ni and U were excluded as being too far from the initial fitted line and therefore not "typical". The preliminary fit, including 12 materials, gave $7.4 10^{10} Z^{(0.79 \pm 0.08)}$.

At lower E_0 , the Z-dependence increases significantly. For example, a fit to the yields calculated for the same 10 materials at $E_0 = 34$ MeV gives a steeper logarithmic slope: $Z^{(1.16 \pm 0.06)}$. The behavior at all E_0 is in fact quite different from that derived from Approximation A together with the empirical behavior of the photoneutron cross

sections: $Y(\text{neutrons s}^{-1} \text{ kW}^{-1}) = 4 \cdot 10^{12} Z^{-1/3}$. (****) The

(****) The integral of the photoneutron cross section weighted by k^{-2} has a trend given by $\sigma_{-2} \equiv \int \sigma_n(k) k^{-2} dk = A^{5/3} / 444 \text{ mb/MeV}$ (Be75, Fig. 42). When this is combined with the other factors in Eq. 4, the $Z^{-1/3}$ dependence results.

marked difference in Z-dependence is also reflected in the ratios shown in Fig. 11 and is mainly a result of the correction factors F^e and F^γ (Figs. 1 and 2).

Equation 5 is primarily meant to illustrate the average trend of these results. Whereas the deviation of points used in the 10-material fit is only $\pm 14\%$, Ni and U individually deviate by -35% and $+47\%$, respectively. Examples of other nuclei not studied here that deviate considerably from the overall trend are Ca and Ti (anomalously low neutron production), Be (anomalously high due to low threshold: 1.67 MeV) and the actinides (Ac, Th, Pa, ...) which produce significantly more neutrons than Eq. 5 would predict, owing to photofission. If anything, these examples serve to reinforce the conclusion that low-Z materials are preferred as targets where neutron yields must be minimized, and that actinides should be avoided. Furthermore, the relative dependence of yield on Z becomes enhanced at lower values of E_0 , as Figs. 8 and 9 show.

The energy spectrum of the produced neutrons is not

given by these calculations. However, various measurements indicate that the neutron spectrum from the giant-resonance is reasonably well described as a fission spectrum (NB64, Mu66) if the energy E_0 is at or above the peak of the giant-resonance energy. Assuming a fission spectrum and an isotropic angular distribution for the photoneutrons, we use the conversion factor ($19 \text{ n cm}^{-2} \text{ s}^{-1} = 2.4 \text{ mrem h}^{-1}$ for a ^{252}Cf spectrum (IC73)) to obtain the scale shown on the right-hand side of Fig. 12, which indicates the neutron dose-equivalent rate index in rem per hour at one meter per kW of electron beam power incident on the material in question. Thus Eq. 5 yields the rule of thumb

$$\dot{H}(\text{rem h}^{-1}) = 93 Z^{0.73} P(\text{kW}) / d(\text{m})^2 \quad (\text{RULE OF THUMB}) \quad (6a)$$

where \dot{H} is the dose-equivalent rate, P is the electron beam power in kW and the distance d is specified in meters. These results also confirm the rule of thumb that one kilowatt of electron beam power incident at high energy on high-Z materials (but not actinides), results in a neutron dose-equivalent rate index of about 2200 rem per hour at one meter, unshielded:

$$\dot{H}(\text{rem h}^{-1}) = 2200 P(\text{kW}) / d(\text{m})^2$$

(RULE OF THUMB, HIGH-Z MATERIALS). (6b)

It is reassuring to confirm that, with currently accepted standards for the evaluation of neutron dose equivalent, the dose-equivalent index of low energy neutrons is below that of bremsstrahlung (X-rays), the predominant secondary radiation, by a comfortable margin. If only hydrogenous materials (e. g., concrete or earth) are used for shielding, a facility will always be well shielded for low-energy neutrons if bremsstrahlung is adequately attenuated. However, if reliance is placed on non-hydrogenous materials, as, for example, where some shielding is provided by high Z materials, this assertion must be reexamined. In such cases it may be found that neutrons are a significant component of the radiation field outside the biological shield, even for accelerators operating below the photopion threshold.

Regardless of the strength or composition of the shielding, neutrons are notoriously capable of finding their way through penetrations and labyrinths. The data given here may safely be used to derive a source term for the calculation of ducting for accelerator installations of any energy.

CONCLUSIONS

The availability of suitable cross section information and a well-grounded theory for the transport of high-energy electromagnetic radiation have made possible the calculation of reliable estimates of neutron yields in a manner that also allows useful statements to be made concerning production systematics. Moreover, the accuracy is certainly sufficient in the entire energy range where low energy photoneutrons are likely to be a significant radiation protection consideration. These yields exhibit a regularity which should simplify radiation protection planning for such accelerator facilities.

The method described has a further obvious use -- the calculation of activity induced by electron beams. A paper describing such predictions is now in preparation.

ACKNOWLEDGEMENTS

Neutron production by electron beams has also been calculated for comparable conditions by several other workers not previously cited (see, for example, Ga69a, Ga69b, Le50, De69, Al70), and the author is indebted to them for the guidance provided by their earlier discussions. Helpful discussions with M. L. Berger, B. L. Berman, E. G. Fuller and G. Luxton are gratefully acknowledged.

REFERENCES

- Al66 Alsmiller R. G. Jr. and Moran H. S., 1966,
Electron-Photon Cascade Calculations and Neutron Yields
from Electrons in Thick Targets, Oak Ridge National
Laboratory, Report No. ORNL-TM 1502; also see, 1967, Nucl.
Instr. Meth. 48, 109.
- Al67 Alsmiller R. G. Jr. and Moran H. S., 1967,
"Photoneutron Production from 34- and 100-MeV Electrons in
Thick Uranium Targets," Nucl. Instr. Meth. 51, 339.
- Al70 Alsmiller R. G. Jr., Gabriel T. A. and Guthrie M. P.,
1970, "The Energy Distribution of Photoneutrons Produced by
150-MeV Electrons in Thick Beryllium and Tantalum Targets,"
Nucl. Sci. Eng. 40, 365.
- Ba59 Barber W. C. and George W. D., 1959, "Neutron Yields
from Targets Bombarded by Electrons," Phys. Rev. 116, 1551.
- Ba67 Bathow G., Freytag E. and Tesch K., 1967,
"Measurements on 6.3 GeV Electromagnetic Cascades and
Cascade-Produced Neutrons," Nucl. Phys. B2, 669.
- Ba69 Barbier M., 1969, Induced Radioactivity, Ch. 5, North-
Holland Publishing Co, Amsterdam, and John Wiley and Sons,
Inc., New York.
- Be64 Berger M. J. and Seltzer S. M., 1964, Tables of Energy
Losses and Ranges of Electrons and Positrons, National
Aeronautics and Space Administration, Report No. NASA
SP-3012, Washington, D. C.
- Be68 Bergère R., Beil H. and Veyssière A., 1968,
"Photoneutron Cross Sections of La, Tb, Ho and Ta," Nucl.

Phys. A121, 463.

Be70 Berger M. J. and Seltzer S. M., 1970, "Bremsstrahlung and Photoneutrons from Thick Tungsten and Tantalum Targets," Phys. Rev. C2, 621.

Be71 Beil H., Bergère R., Carlos P., Leprêtre A., Veyssière A. and Parlag A., 1971, "Giant Dipole Resonance in $N = 82$ Nuclei," Nucl. Phys. A172, 426.

Be75 Berman B. L. and Fultz S. C., 1975, "Measurements of the Giant Dipole Resonance with Monoenergetic Photons," Rev. Mod. Phys. 47, 713.

Be76 Berman B. L., 1976, Atlas of Photoneutron Cross Sections Obtained with Monoenergetic Photons, Bicentennial Edition, Lawrence Livermore Laboratory, Report No. UCRL-78482. Also see 1975, "Atlas of Photoneutron Cross Sections Obtained with Monoenergetic Photons," Atomic Data and Nuclear Data Tables 15, 319.

Ca76 Caldwell J. T., Dowdy E. J., Berman B. L., Alvarez R. and Meyer P., 1976, Photonuclear Measurements on Fissionable Isotopes using Monoenergetic Photons, Los Alamos Scientific Laboratory, Report No. LA-UR-76 615, Los Alamos, N. M.

De63 DeStaebler H., 1963, Photon-Induced Residual Activity, Stanford Linear Accelerator Center, Report No. SLAC-TN-6392, Stanford, CA.

De68 DeStaebler H., Jenkins T. M. and Nelson W. R., 1968, "Shielding and Radiation," Ch. 26, The Stanford Two-Mile Accelerator (Neal R. B., Gen. Ed.), Benjamin, New York.

- De69 Dealler J. F. B., 1969, "Photoneutron Production in Thick Bremsstrahlung Targets," Health Physics 16, 238.
- Fu62 Fuller E. G. and Hayward E., 1962, "The Photodisintegration of Bismuth and the Lead Isotopes," Nucl. Phys. 33, 431.
- Fu64 Fultz S. C., Bramblett R. L., Caldwell J. T. and Harvey R. R., 1964, "Photoneutron Cross Sections for Natural Cu, Cu⁶³, and Cu⁶⁵," Phys. Rev. 133, B1149.
- Fu66 Fultz S. C., Caldwell J. T., Berman B. L., Bramblett R. L. and Harvey R. R., 1966, "Photoneutron Cross Sections for C¹² and Al²⁷," Phys. Rev. 143, 790.
- Fu74 Fultz S. C., Alvarez R. A., Berman B. L. and Meyer P., 1974, "Photoneutron Cross Sections of ⁵⁸Ni and ⁶⁰Ni," Phys. Rev. C10, 608.
- Fu76 Fuller E. G. and Hayward E., 1976, Photonuclear Reactions, Dowden, Hutchinson and Ross, Inc., Shrodsberg, PA.
- Fu77 Fuller E. G., 1977, private communication, National Bureau of Standards, Washington, D. C.
- Ga57 Gavrilov B. I. and Lazareva L. E., 1957, "Yields of Photoneutrons from Intermediate and Heavy Nuclei," J. Exptl. Theoret. Phys. (U. S. S. R.); trans.: 1957, Sov. Phys. JETP 3, 871.
- Ga69a Gabriel T. A. and Alsmiller R. G. Jr., 1969, Photonucleon and Photopion Production from High-Energy (50 to 400 MeV) Electrons in Thick Copper Targets, Oak Ridge National Laboratory, Report No. ORNL-4443, Oak Ridge, TN.

- Ga69b Gabriel T. A. and Alsmiller R. G. Jr., 1969,
"Photonucleon and Photopion Production from 400 MeV
Electrons in Thick Copper Targets," Nucl. Phys. B14, 303.
- Ha64 Harvey R. R., Caldwell J. T., Bramblett R. L. and
Fultz S. C., 1964, "Photoneutron Cross Sections of Pb²⁰⁶,
Pb²⁰⁷, Pb²⁰⁸, and Bi²⁰⁹," Phys. Rev. 136, B126.
- Ha75 Hansen E. C., Bartoletti C. S. and Daitch P. B., 1975,
"Analog Monte Carlo Studies of Electron-Photon Cascades and
the Resultant Production and Transport of Photoneutrons in
Finite Three-Dimensional Systems," J. Appl. Phys. 46, 1109.
- Hu69 Hubbell J. H., 1969, Photon Cross Sections,
Attenuation Coefficients and Energy Absorption Coefficients
from 10 keV to 100 GeV, National Bureau of Standards,
Report No. NSRDS-NBS 29, Washington, D. C.
- IC73 International Commission on Radiological Protection,
1973, Data for Protection Against Ionizing Radiation from
External Sources: Supplement to ICRP Publication 15, ICRP
Publication No. 21, Pergamon Press, Oxford, Table 9, p. 19.
- Jo53 Jones L. W. and Terwilliger K. M., 1953, "Photoneutron
Production Excitation Functions to 320 MeV," Phys. Rev. 91,
699.
- Le50 Levinger J. S., 1950, "Neutron Production by Complete
Absorption of High-Energy Photons," Nucleonics, May, 1950,
64.
- Le74 Leprêtre A., Beil H., Bergère R., Carlos P., de Miniac
A., Veyssière A. and Kernbach K., 1974, "A Study of the
Giant Dipole Resonance of Vibrational Nuclei in the $103 \leq A$

- ≤ 133 Mass Region," Nucl. Phys. A219, 39.
- Mi62 Miller J., Schuhl C. and Tzara C., 1962, "Mesure des Sections Efficaces (γ , n) de Cu, Ce, La, Ta, Au, Pb et Bi en Valeur Absolue," Nucl. Phys. 32, 236.
- Mo53 Montalbetti R., Katz L. and Goldemberg J., 1953, "Photoneutron Cross Sections," Phys. Rev. 91, 659.
- Mu66 Mutchler G. S., 1966, The Angular Distributions and Energy Spectra of Photoneutrons from Heavy Elements, Ph. D. Thesis, Massachusetts Institute of Technology, Report No. MIT-2098-224, available from E. R. D. A. Technical Information Center, P. O. Box 62, Oak Ridge, TN.
- NB64 National Bureau of Standards, National Council on Radiation Protection and Measurements, 1964, Shielding for High-Energy Electron Accelerator Installations, NBS Handbook No. 97 and NCRP Report No. 31, Washington, D. C., Fig. 15, p. 25.
- Pr50 Price G. A. and Kerst D. W., 1950, "Yields and Angular Distributions of Some Gamma-Neutron Processes," Phys. Rev. 77, 806.
- Ro41 Rossi B. and Greisen K., 1941, "Cosmic Ray Theory," Rev. Mod. Phys. 13, 240.
- Ro52 Rossi B., 1952, High-Energy Particles, Prentice-Hall, Inc., Englewood Cliffs, N. J., Ch. 5.
- Sw75 Swanson W. P., 1975, "Activation of Aluminum Beam Dumps by High-Energy Electrons at SLAC," Health Physics 28, 495.
- Ta39 Tamm Ig. and Belenky S., 1939, "On the Soft Component

of Cosmic Rays at Sea Level," Journal of Physics (U.S.S.R.)
I, 177.

Te76 Tesch K., 1976, private communication, Deutsches
Elektronen-Synchrotron DESY, Hamburg.

Ts74 Tsai Y.-S., 1974, "Pair Production and Bremsstrahlung
of Charged Leptons," Rev. Mod. Phys. 46, 828.

Ve70 Veyssièrè A., Beil H., Bergèrè R., Carlos P. and
Leprêtrè A., 1970, "Photoneutron Cross Sections of ^{208}Pb
and ^{197}Au ," Nucl. Phys. A159, 561.

Ve73 Veyssièrè A., Beil H., Bergèrè R., Carlos P., Leprêtrè
A. and Kernbach K., 1973, "A Study of the Photofission and
Photoneutron Processes in the Giant Dipole Resonance of
 ^{232}Th , ^{238}U and ^{237}Np ," Nucl. Phys. A199, 45.

Ve74 Veyssièrè A., Beil H., Bergèrè R., Carlos P., Leprêtrè
A. and de Miniac A., 1974, "A Study of the Photoneutron
Contribution to the Giant Dipole Resonance of s-d Shell
Nuclei," Nucl. Phys. A227, 513.

Ve75 Veyssièrè A., Beil H., Bergèrè R., Carlos P., Leprêtrè
A. and de Miniac A., 1975, "Étude de la Résonance Géante
Dipolaire dans la Région de Transition autour de $A = 190$,"
J. Physique 36, L-267.

Ze62 Zerby C. D. and Moran H. S., 1962, Studies of the
Longitudinal Development of High-Energy Electron Photon
Cascade Showers in Copper, Oak Ridge National Laboratory,
Report No. ORNL-3329, Oak Ridge, TN; see also 1963,
"Studies of the Longitudinal Development of Electron-Photon
Cascade Showers," J. Appl. Phys. 34, 2445.

FIGURE CAPTIONS

1. Examples of the factor F^e used to correct for the actual amount of radiation per unit electron track length at kinetic energy E , relative to the amount at infinite energy. At the high-energy limit, all curves tend towards unity. Factor is derived from values of $dE/dL(\text{rad})$ published by Berger and Seltzer (Be74).

2. Examples of the factor F^γ , used to correct for the actual photon track length at energy k , relative to the track length at infinite energy. At the high-energy limit, all curves tend towards unity. Factor is derived from values of μ/ρ published by Hubbell (Hu69). Photoneutron thresholds are indicated as solid circles.

3. Electron differential track length for four materials for incident electron kinetic energy $E_0 = 20$ MeV. The fractions at the right indicate that each curve approaches $1/\epsilon_0$ at $E = E_0$. The curve corresponding to the arbitrarily small value $\epsilon_0 = 1$ MeV may be compared with the straight line of slope -2 from Approximation A (see text for discussion).

4. Photon differential track length for ten materials, for incident electron energy $E_0 = 20$ MeV. Photoneutron thresholds are indicated by closed circles. Choice of dimensionless ordinate variable is explained in text. The Approximation A value, valid for all energies and materials, is indicated at 0.572 for comparison.

5. Photon differential track length for Pb for incident electron kinetic energies in the range $E_0 = 5 - 35$ MeV. The Approximation A result is indicated at 0.572 for comparison. The photoneutron cross section (barns), containing the neutron multiplicity, is also shown (smoothed). Threshold is indicated as k_{th} . Also shown are Monte-Carlo calculations for 34 MeV electrons ($10 X_0$ Pb) (Al66).

6. Photon differential track length and photoneutron cross section for Cu. Also shown are the Approximation A prediction and a Monte-Carlo calculation for $E_0 = 34$ MeV ($5 X_0$ Cu) (Al66). With Approximation B plotted in this manner, initial slopes of all curves are approximately equal to $(9/7)$ ($1/\epsilon_0$), and the final slopes are equal in magnitude to this but of opposite sign.

7. Same as for Figs. 5 and 6 but for Al.

8. Neutron yields from semi-infinite targets of twelve natural materials per unit incident electron beam power, plotted as a function of incident electron energy E_0 . Threshold for each material is indicated as a closed circle. See Table 1 for sources of cross section data and text for discussion of accuracy.

9. As for Fig. 8, extended to $E_0 = 100$ MeV.

10. Relative yields of neutrons released by electron beams incident on Pb targets at energies $E_0 = 100, 34$ and 17 MeV, and Cu at 34 MeV (dashed), as functions of target thickness in radiation lengths X_0 . The curves are qualitatively similar for other materials and energies, but the central portion (as represented, say, by the point at which the relative

yield is 0.5) is displaced from the curve for Pb at 100 MeV by an increment in X/X_0 roughly equal to $\ln(E_0/\epsilon_0) - 2.35$. Curves for Pb at 34 and 100 MeV are averages adapted from Alsmiller et al. (Al66) and Hansen et al. (Ha75). Curve for 17 MeV is an interpolation. Curve for Cu at 34 MeV (based on the cited work but extrapolated to targets thicker than $5 X_0$ using the photon mass attenuation coefficient for $k = 17$ MeV) is almost identical to the 17-MeV curve for Pb.

11. Ratio of neutron yield from semi-infinite targets according to the calculation described, to the yield that would be predicted by Approximation A (Eq. 4), plotted as a function of atomic number Z . Curves are interpolations of calculated points and parameter affixed to each curve is the incident electron energy E_0 . Points are the same at $E_0 = 500$ and 1000 MeV, and there is no reason to expect a significant change at higher E_0 . The Z -intercept for each energy is given by $k_{th}(Z) = E_0$.

12. Neutron yield from semi-infinite targets (neutrons per second per kW of incident electron beam power), at saturation ($E_0 = 500 - 1000$ MeV, Table 2) plotted as a function of target atomic number. The right-hand scale, which gives the dose-equivalent rate index at 1 meter from the target, is related to the left-hand scale by means of the fluence to dose-equivalent conversion recommended by the ICRP (IC73) for a ^{252}Cf spectrum, assuming isotropic neutron production. Straight line is a least-squares regression of all points except Ni and U.

TABLE HEADINGS

1. Material Constants Used.
2. Comparison with Measurements and Other Calculations
for Thick Targets ($\gtrsim 3 X_0$).

Table 1. Material Constants Used.

Z	Material	$k_{th}^{(a)}$ (MeV)	Radiation Length ^(b) ρX_0 (g cm ⁻²)	Critical Energy (MeV X_0^{-1})		$X_p/X_0^{(d)}$	References for Cross Sections (k < 30 MeV)
				As Defined	Used ^(c)		
6	Carbon	18.72	42.70	97.1	79.38	1.287	Fu66 ^(e)
13	Aluminum	13.03	24.01	51.0	41.95	1.306	Ve74
26	Iron	11.21	13.84	27.4	22.31	1.295	Mo53, Pr50 ^(f)
28	Nickel	11.38	12.68	25.6	21.00	1.299	Fu74
29	Copper	9.91	12.86	24.8	20.23	1.300	Fu64
47	Silver	9.18	8.97	16.2	13.32	1.293	Le74
56	Barium	6.90	8.31	15.1	12.11	1.293	Be71
73	Tantalum	7.64	6.82	10.4	9.11	1.297	Be68
74	Tungsten	6.20	6.76	10.2	9.02	1.297	Ve75
79	Gold	8.07	6.46	9.66	8.55	1.297	Ve70
82	Lead	6.73	6.37	9.51	8.50	1.298	Ha64, Ve70 ^(g)
92	Uranium	6.04	6.00	8.36	7.64	1.292	Ve73 ^(h)

- (a) In determining threshold energies, isotopes constituting less than 1% of the natural material are disregarded.
- (b) Radiation lengths are obtained from Tsai (Ts74).
- (c) The values of the "critical energy" actually used for calculation were obtained from $X_0 dE/dX(\text{col})$, where $dE/dX(\text{col})$ was determined at 30 MeV for each material (Be64). The choice of energy used for determining ϵ_0 is somewhat arbitrary because $dE/dX(\text{col})$ varies slowly over the energy range considered, and 30 MeV was chosen as "typical" of the energy range in which ϵ_0 has an important effect; at higher energies ϵ_0 becomes less significant. The values used may be compared with the actual critical energies, defined as in the text and interpolated from the tables of Berger and Seltzer (Be64).
- (d) The ratio X_p/X_0 was determined for each material from the tabulations of Hubbell (Hu69) for $k = 100$ GeV. Note that all values are close to the nominal $9/7 = 1.286 \dots$
- (e) The cross sections from the source quoted have been scaled by a factor of 1.22 (Fu77).
- (f) Resonance parameters for Fe are taken from Montalbetti et al. (Mo53). Overall normalization is arbitrarily scaled to bring the Fe/Cu yield ratio into agreement with Price and Kerst (Pr50).
- (g) For ^{208}Pb : Ve70; for ^{206}Pb and ^{207}Pb : Ha64.
- (h) Neutron multiplicity for photofission $\bar{v} = 1.862 + 0.1234 k(\text{MeV})$ taken from Caldwell et al. (Ca76).

Table 2. Comparison with Measurements and Other Calculations for Thick Targets ($\geq 3 X_0$). (*)

Natural Material and Source of Data(**)	Yield (10^{12} neutrons s^{-1} kW^{-1}) and Target Thickness (X_0)				
	34 MeV	100 MeV	500 MeV	1000 MeV	6.3 GeV
Carbon					
(a) This work (C: ∞X_0) (***)	0.097	0.31	0.38	0.38	
Aluminum					
(a) Bathow et al. (M: Ba67, Te76) (****)					1.1 (18)
(b) This work (***)	0.22	0.50	0.56	0.56	
Iron					
(a) This work (***)	0.51	0.72	0.76	0.76	
Nickel					
(a) This work (***)	0.37	0.62	0.68	0.68	
Copper					
(a) Alsmiller & Moran (C: Al66, Fig. 8: Fu64)	0.51 (5)				
(b) Corr'd via Fig. 10, this work (1/0.88)	0.58 (10)				
(c) Hansen et al. (C: Ha75, Table I: Fu64)	0.49 (5)				
(d) Corr'd via Fig. 10, this work (1/0.88)	0.56 (10)				
(e) Barber & George (M: Ba59, Fig. 6)	0.54 (3.13)				
(f) Corr'd via Fig. 10, this work (1/0.74)	0.73 (10)				
(g) Barber & George (M: Ba59, Fig. 6)	0.61 (4.17)				
(h) Corr'd via Fig. 10, this work (1/0.83)	0.73 (10)				
(i) Bathow et al. (M: Ba67, Te76) (****)					2.2 (17)
(j) This work (C: CRS sctns of Fu64 to 34 MeV)	0.73				
(k) This work (***)	0.74	1.03	1.08	1.08	
Silver					
(a) This work (***)	1.28	1.56	1.67	1.67	
Barium					
(a) This work (***)	1.58	1.84	1.94	1.94	
Tantalum					
(a) Alsmiller & Moran (C: Al66, Fig. 11)		2.08 (10)			
(b) Alsmiller & Moran (C: Al66, Table 2) (*****)	1.53 (10)	2.02 (20)			
(c) Hansen et al. (C: Ha75, Table III)		2.13 (10)			
(d) (C: Ha75, Table V)		1.57 (10)			
(e) This work (***)	1.76	2.00	2.13	2.13	
Tungsten					
(a) This work (***)	1.98	2.28	2.42	2.42	
Gold					
(a) This work (***)	1.75	2.00	2.13	2.13	
Lead					
(a) Alsmiller & Moran (C: Al66, Table 2a: Fu62)	2.41 (10)	3.18 (20)			
(b) (C: Al66, Table 2b: Mi62)	1.97 (10)	2.83 (20)			
(c) (C: Al66, Table 2c: Ha64)	1.30 (10)	1.60 (20)			
(d) Hansen et al. (C: Ha75, Tab. VII: Fu62, Jo53)	1.99 (10)	2.39 (10)			
(e) (C: Ha75, Tab. VIII: Mi62, Jo53)	1.48 (10)	1.86 (10)			
(f) (C: Ha75, Table VI: Ha64, Jo53)	1.25 (10)	1.64 (10)			
(g) Barber & George (M: Ba59, Fig. 9)	1.18 (2.98)				
(h) Corr'd via Fig. 10, this work (1/0.69)	1.70 (10)				
(i) Barber & George (M: Ba59, Fig. 9)	1.41 (3.94)				
(j) Corr'd via Fig. 10, this work (1/0.79)	1.78 (10)				
(k) Barber & George (M: Ba59, Fig. 9)	1.64 (5.93)				
(l) Corr'd via Fig. 10, this work (1/0.92)	1.78 (10)				
(m) Bathow et al. (M: Ba67, Te76) (****)					2.6 (12)
(n) This work (C: C.s. of Ha64; Jo53, $k > 22$ MeV)	1.35	1.55			
(o) This work (C: C.s. of Ha64; const: $k > 22$ MeV)	1.49	1.77			
(p) This work (***)	1.60	1.85	1.98	1.98	
Uranium					
(a) Alsmiller & Moran (C: Al67, Fig. 1: Ga57, Jo53)	3.49 (10)	3.93 (10)			
(b) Hansen et al. (C: Ha75, Table XI: Jo53)	3.53 (10)	4.29 (10)			
(c) (C: Ha75, Table XII: Ga57)	2.86 (10)	3.27 (10)			
(d) Barber & George (M: Ba59, Fig. 11)	2.56 (3.46)				
(e) Corr'd via average of (a,b,c) (1/0.77)	3.32 (10)				
(f) This work (***)	3.09	3.40	3.62	3.62	

- (*) For purposes of this work, $10 - 20 X_0$ may be considered equivalent to semi-infinite.
(**) M: Measurement; C: Calculation. For calculated values, reference to source of original cross sections is given following the main reference.
(***) Calculation for semi-infinite targets. For $E_0 = 500$ and 1000 MeV, the integration over photon energy extends only to $k = 150$ MeV.
(****) Measurement of neutrons of energy less than 25 MeV.
(*****) The datum tabulated at $E_0 = 34$ MeV is actually for 30 MeV.

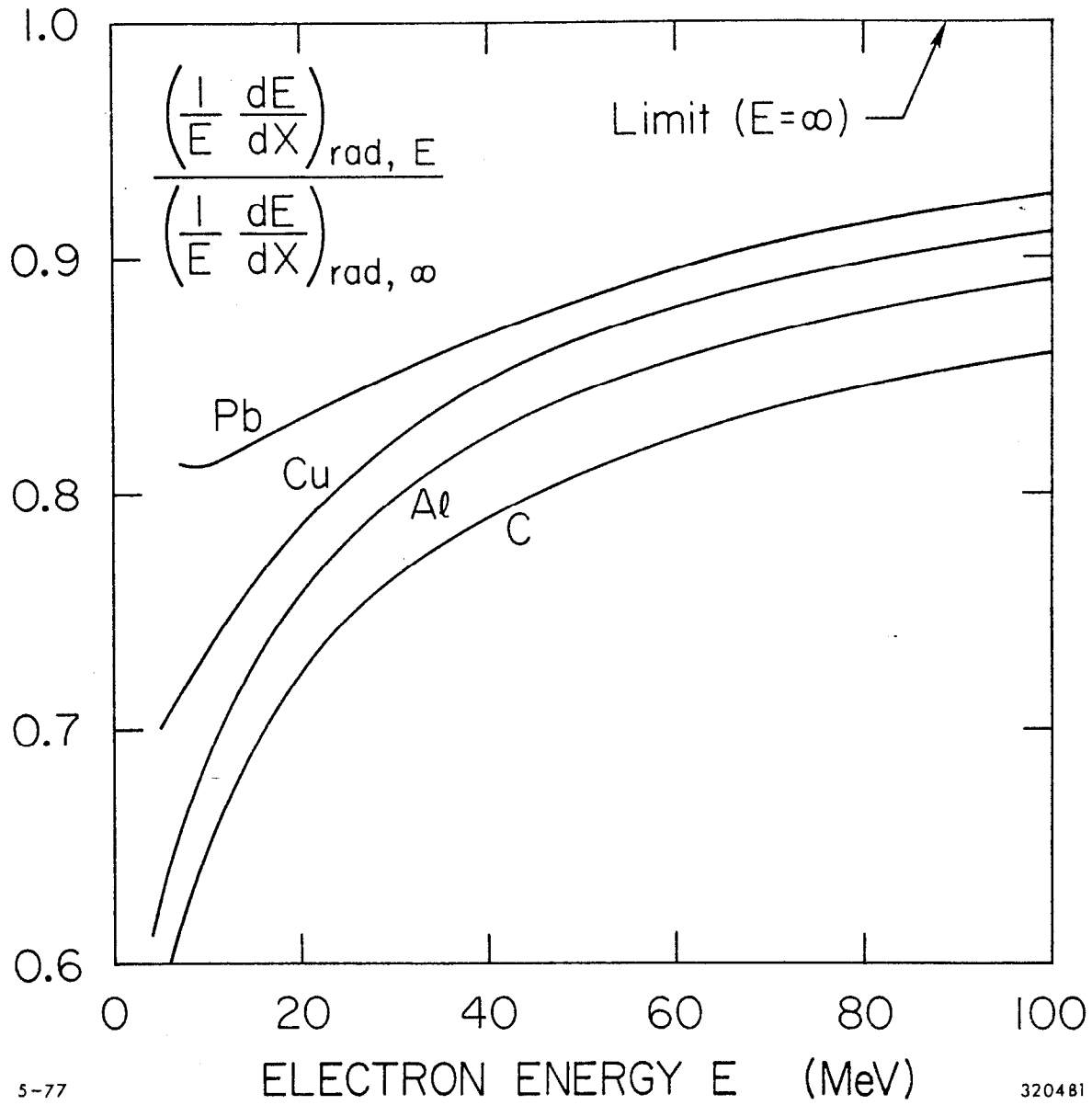


Fig. 1

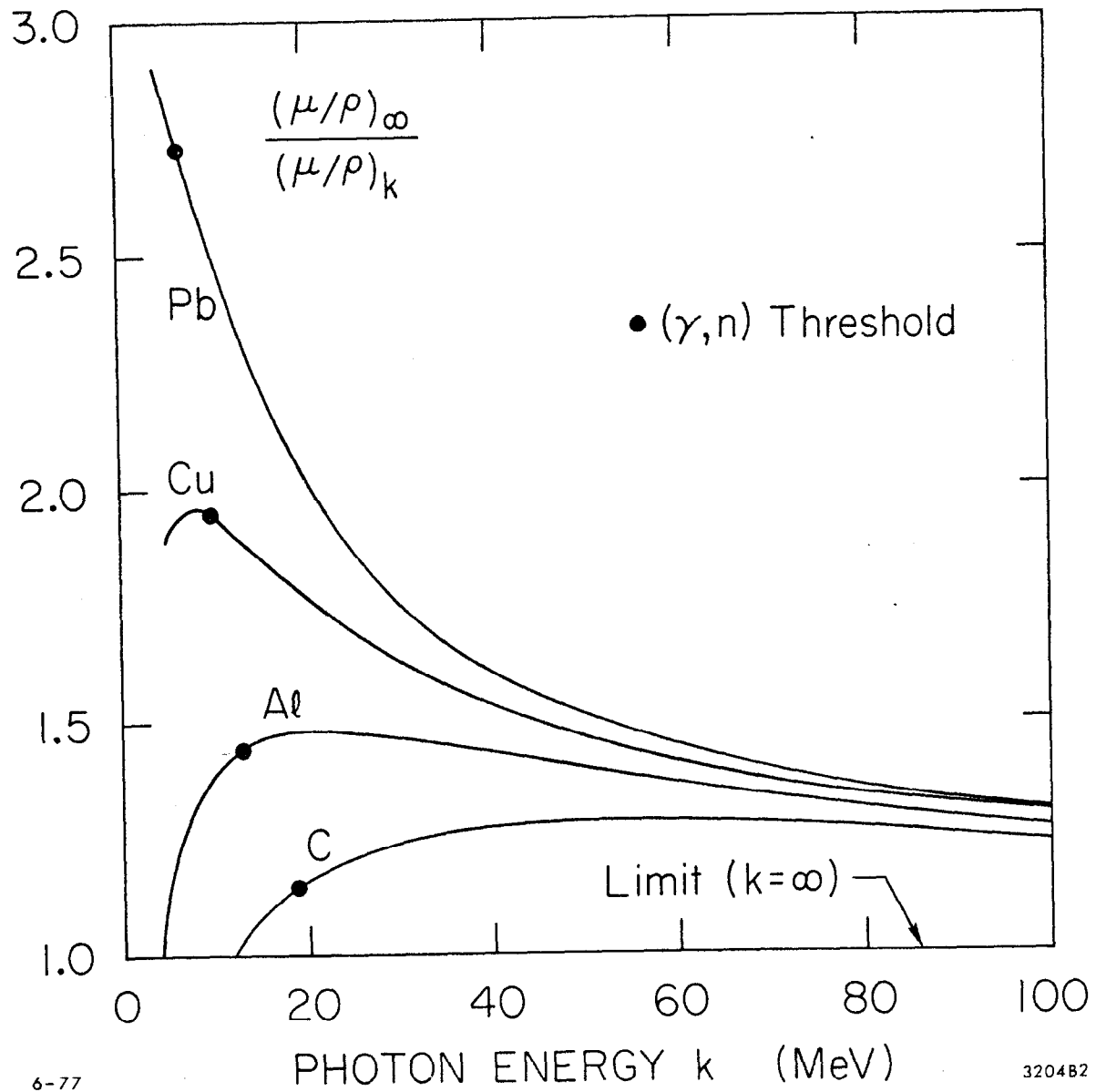


Fig. 2

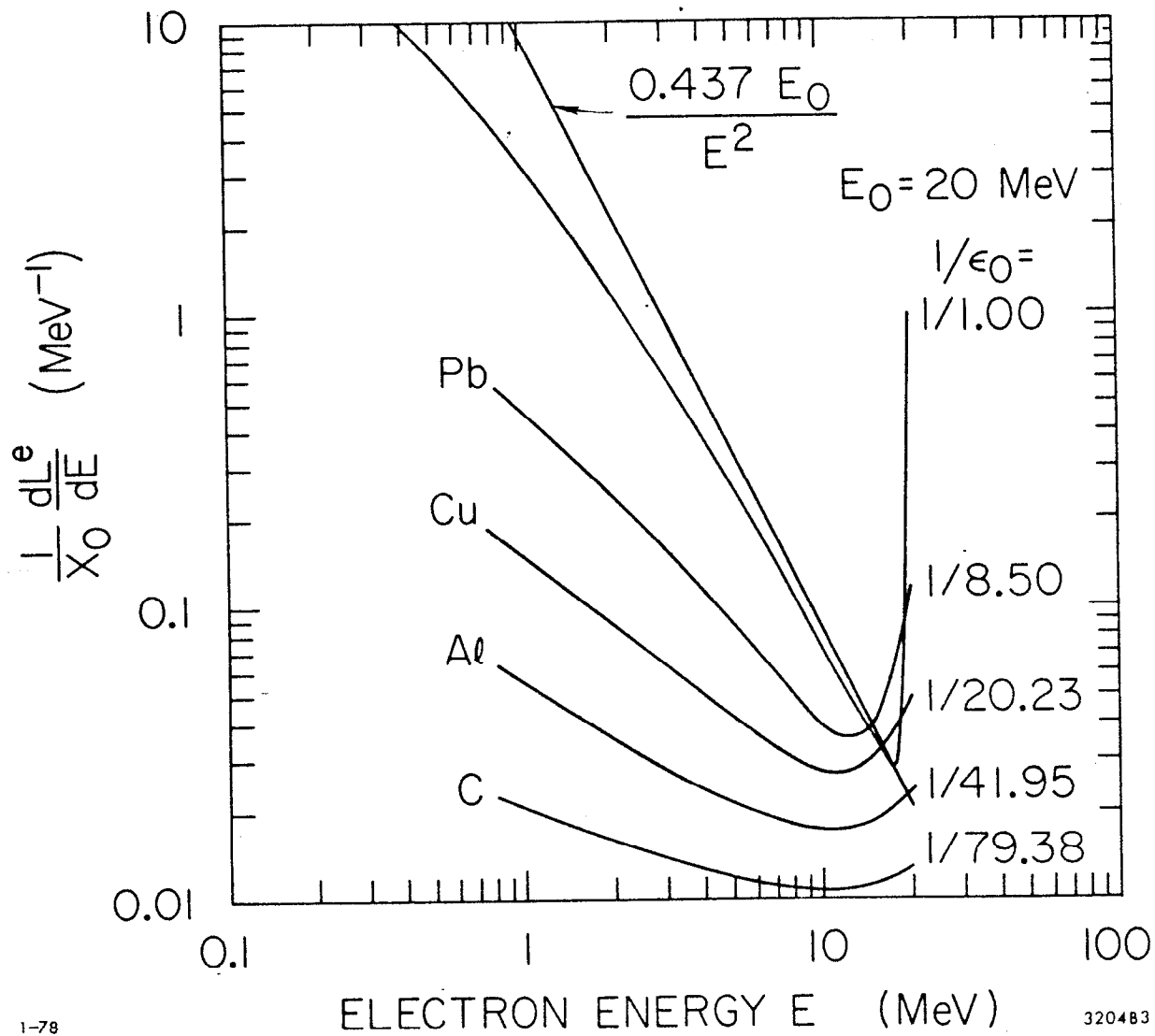


Fig. 3

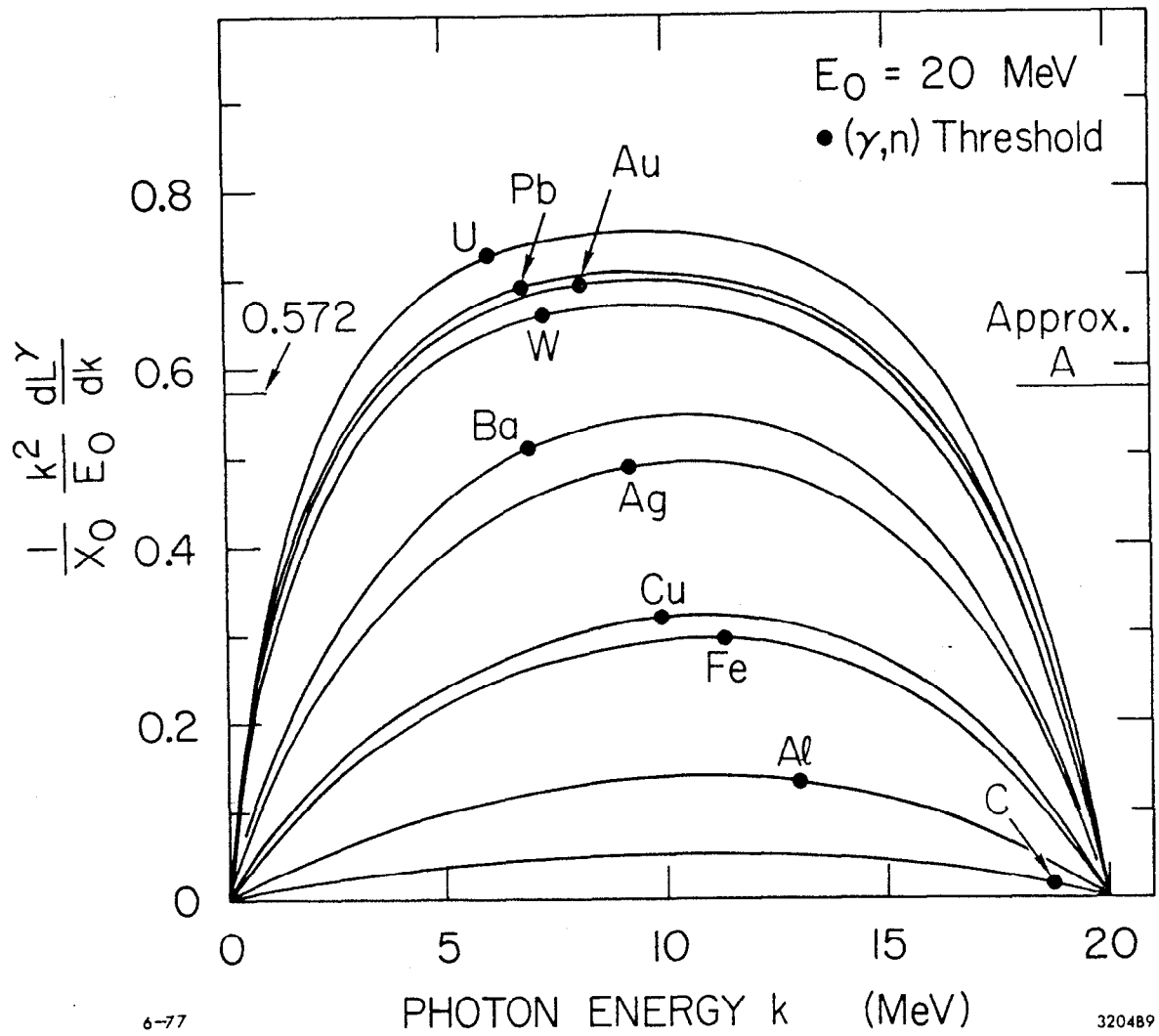


Fig. 4

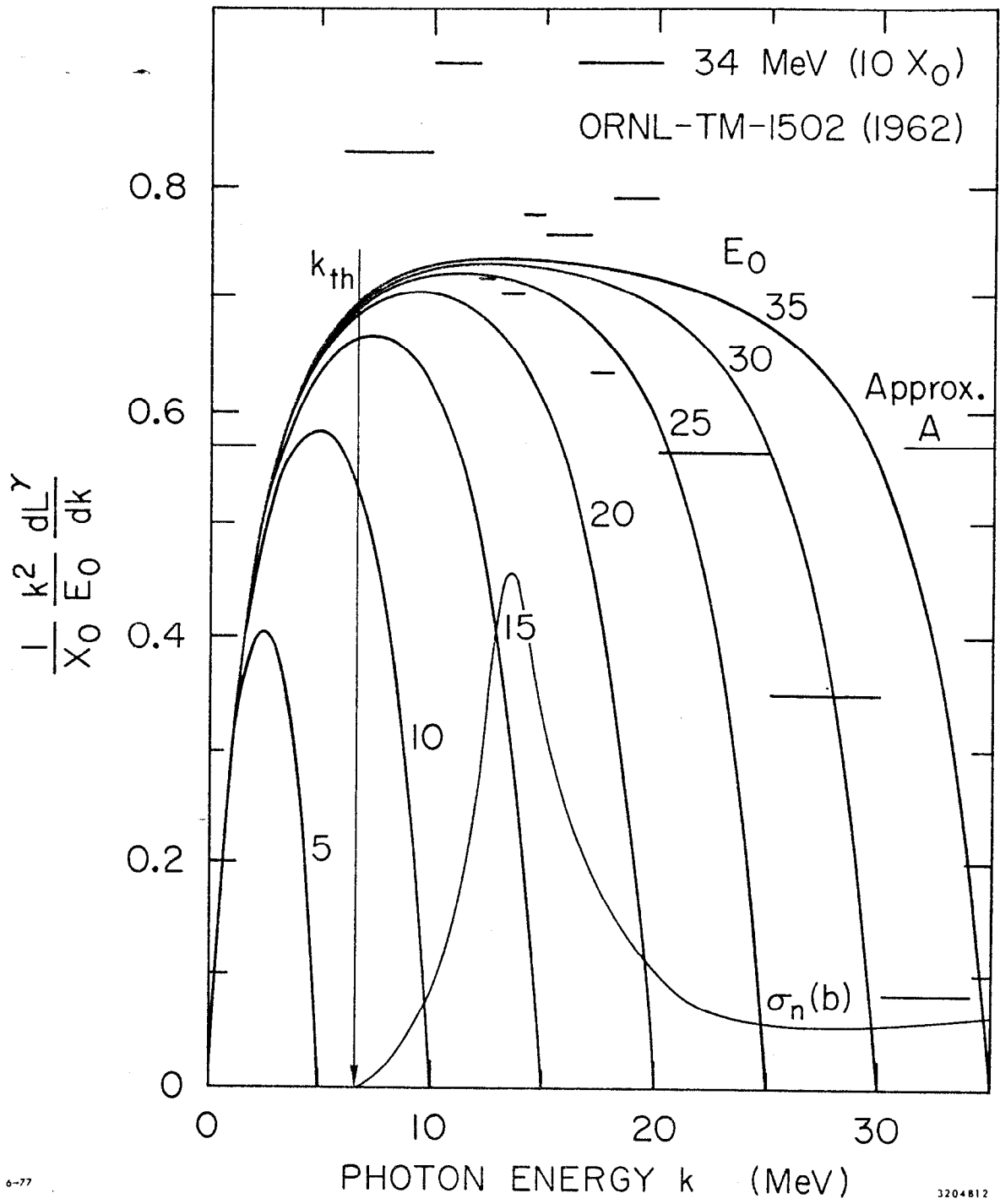


Fig. 5

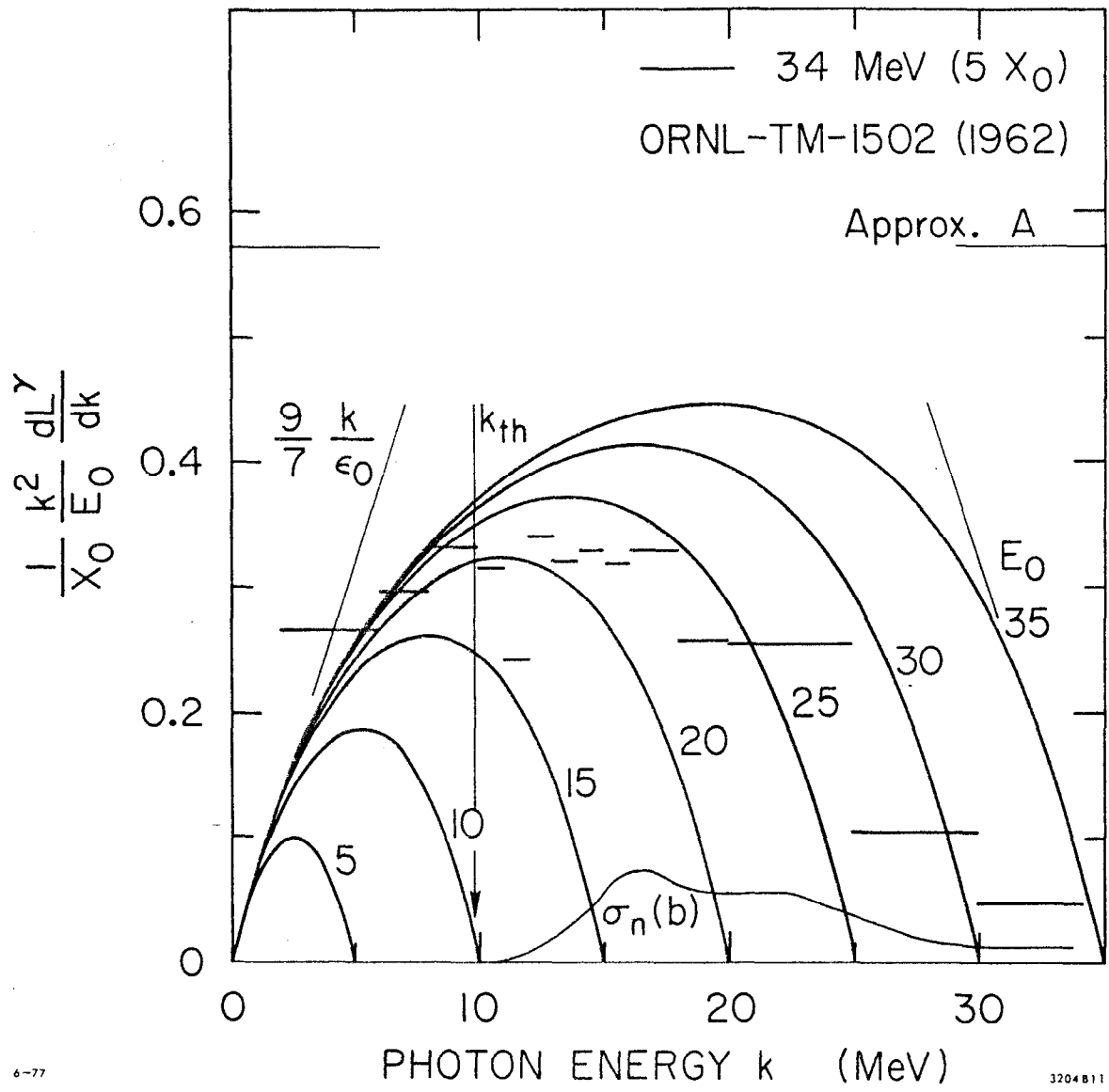
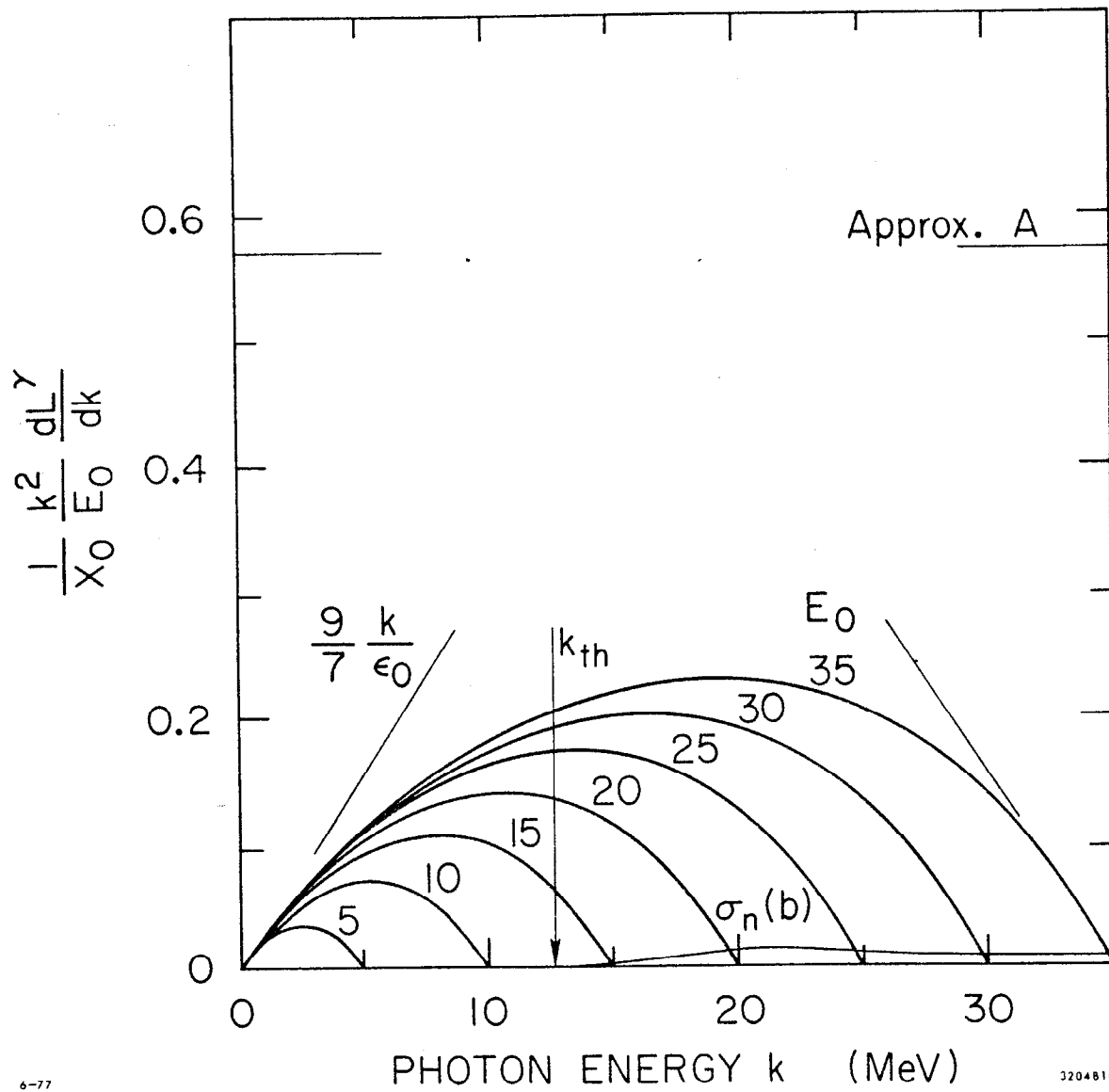


Fig. 6



6-77

3204810

Fig. 7

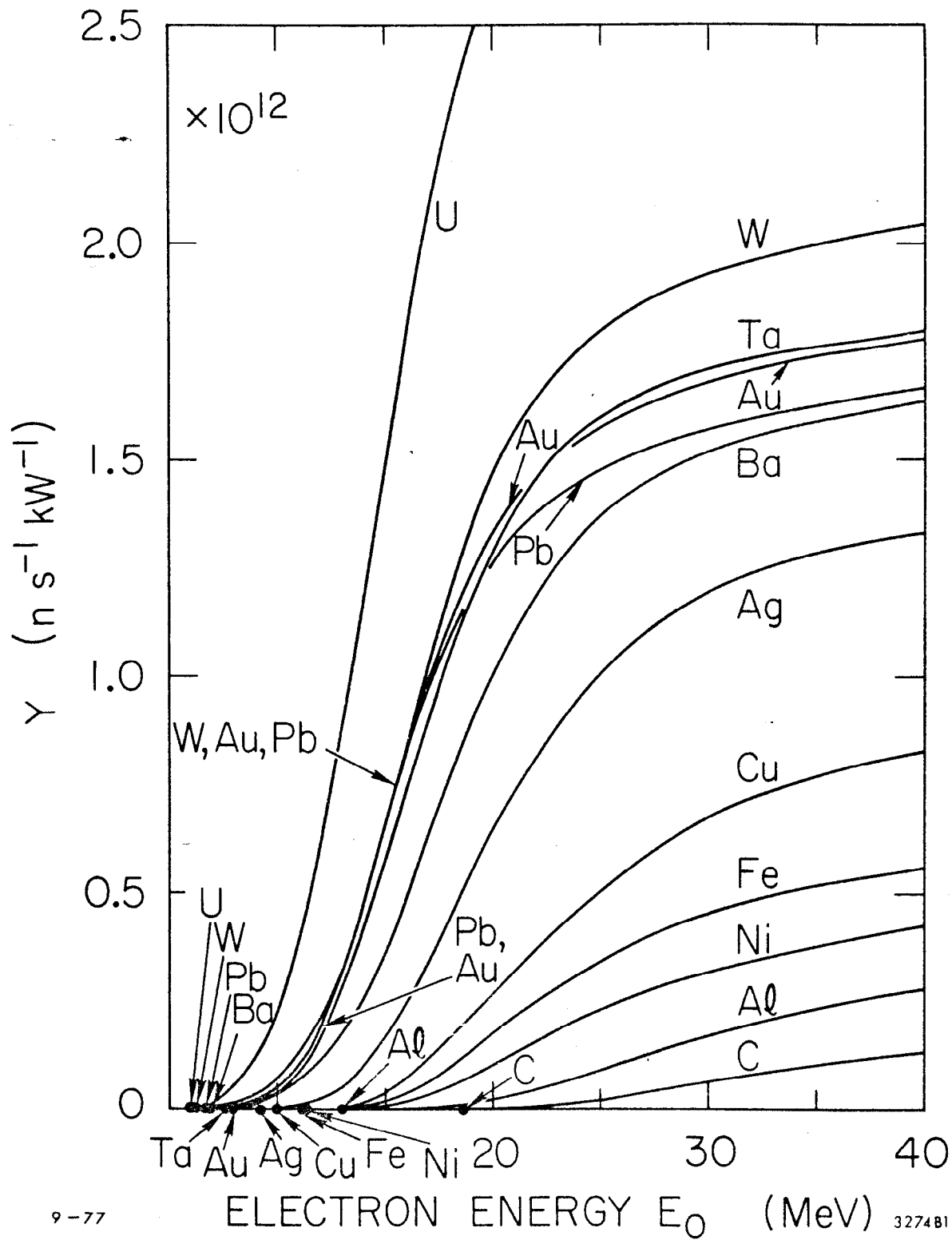


Fig. 8

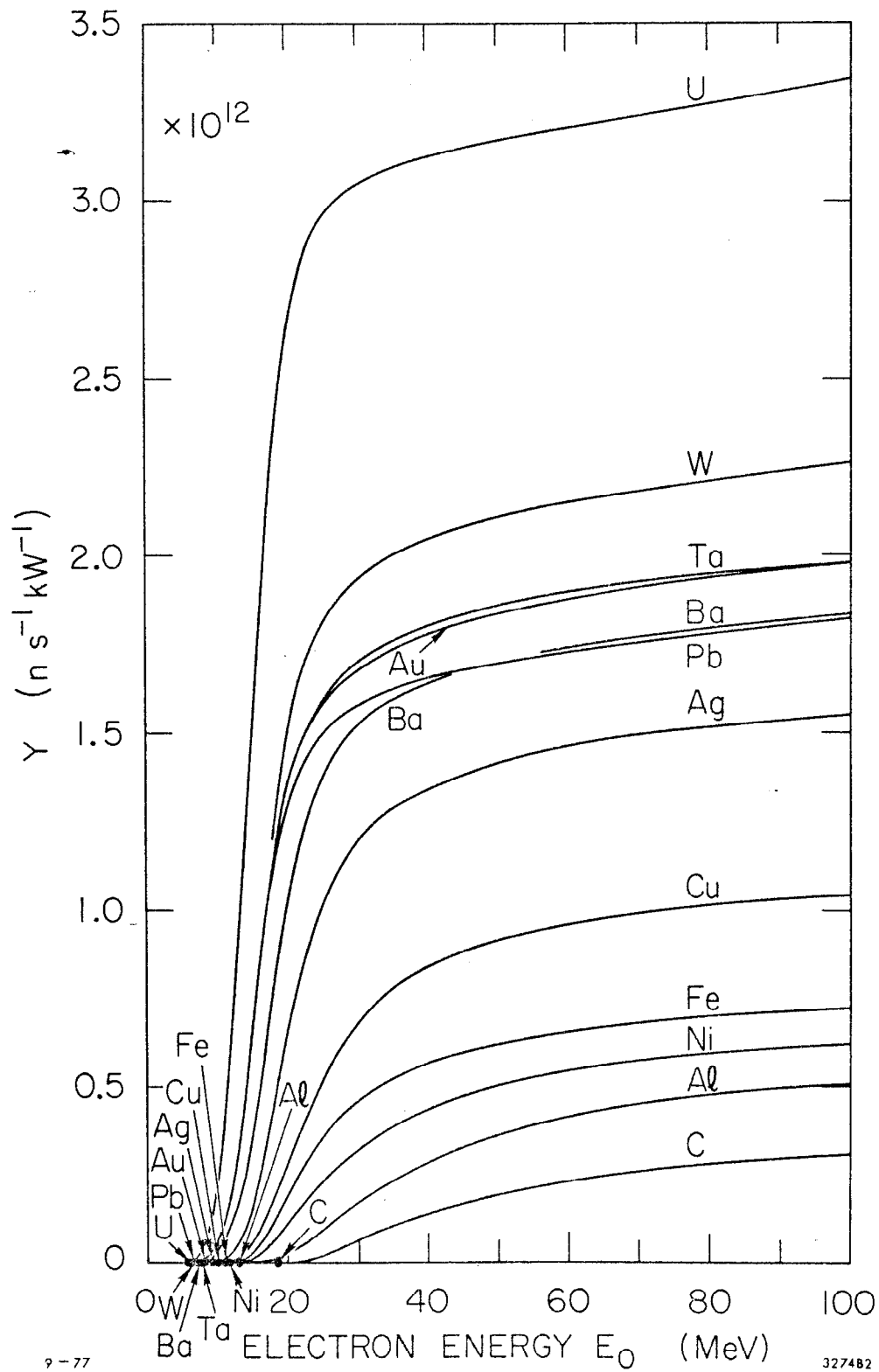


Fig 9

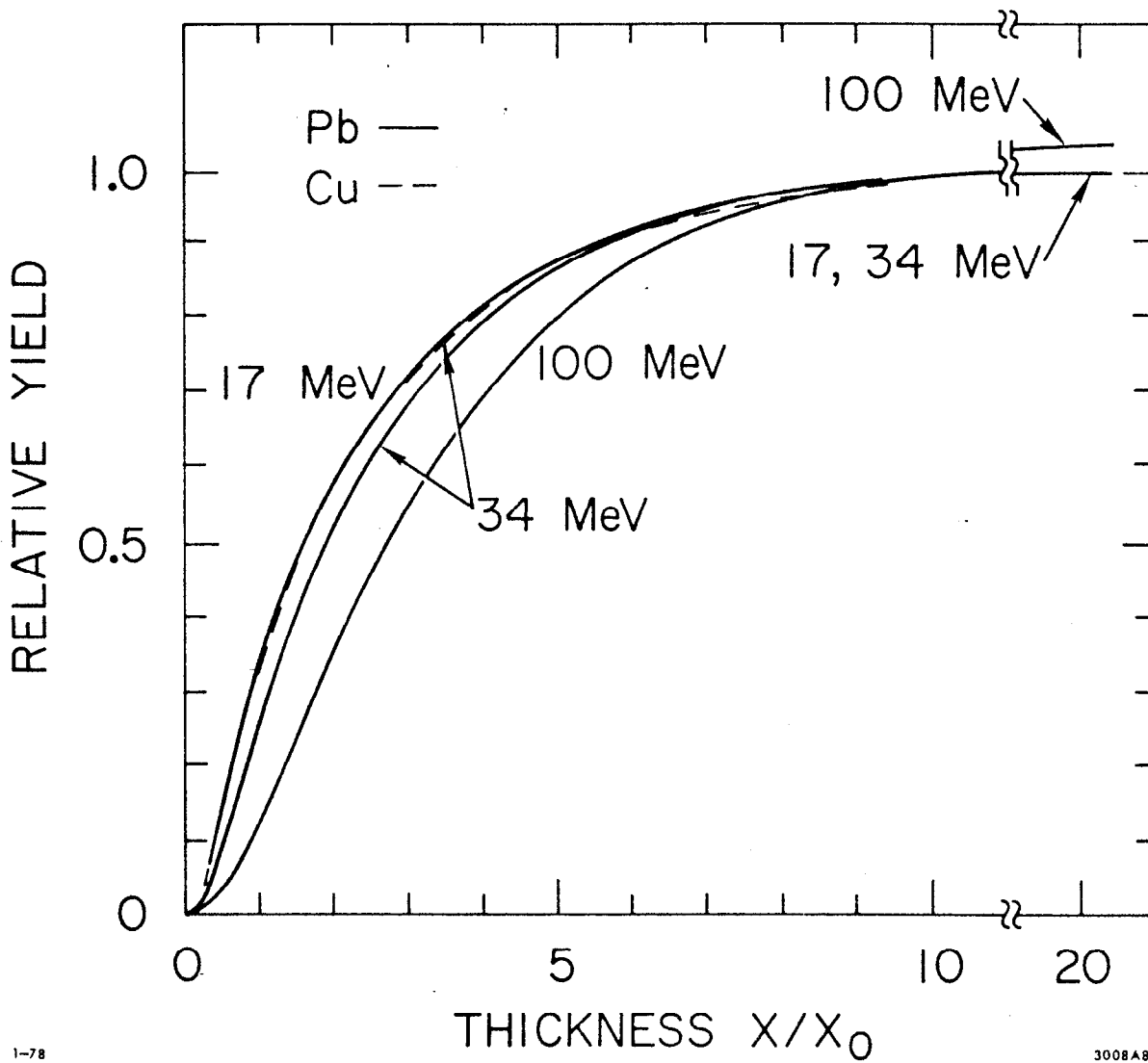


Fig. 10

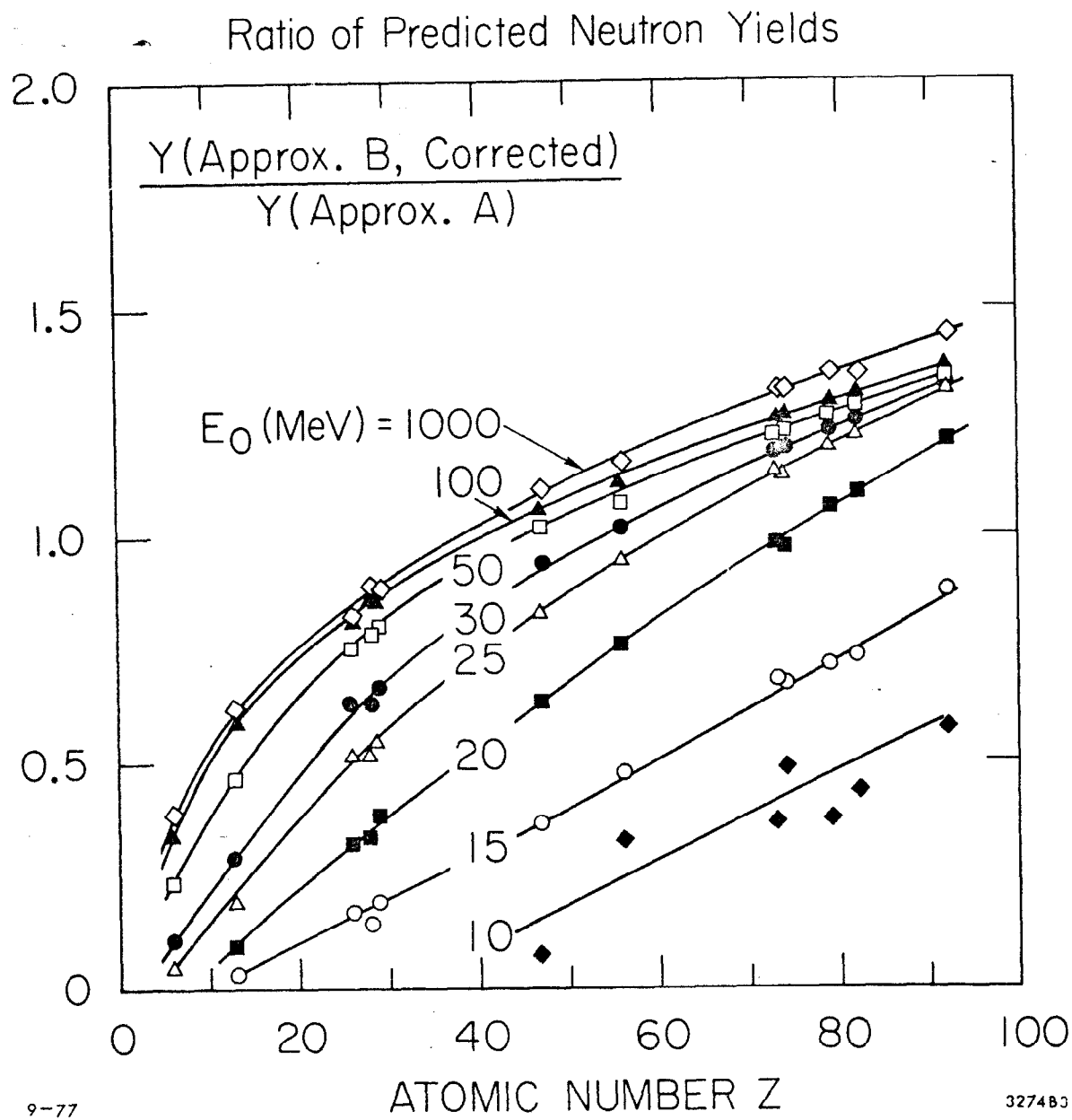
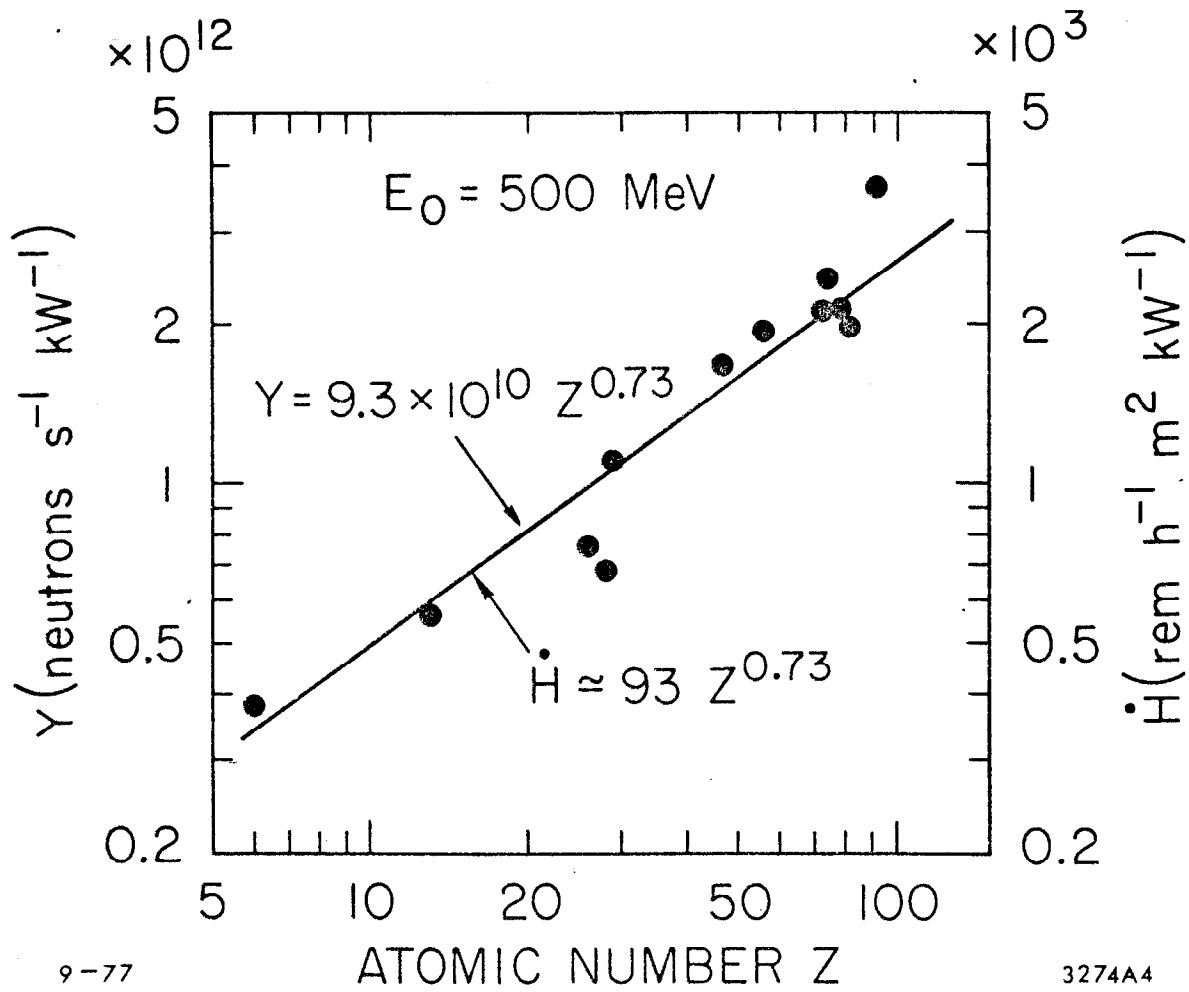


Fig. 11



9-77

3274A4

Fig. 12